Journal of Cluster Science
https://doi.org/10.1007/s10876-022-02382-8

ORIGINAL PAPER

Investigation of the Peculiarities of Oxidation of Ti/Al Nanoparticles on Heating to Obtain TiO_2/Al_2O_3 Composite Nanoparticles

A. S. Lozhkomoev[1] · S. O. Kazantsev[1,2] · O. V. Bakina[1,2] · A. V. Pervikov[1,2] · V. R. Chzhou[1,2] · N. G. Rodkevich[1] · M. I. Lerner[1,2]

Received: 30 August 2021 / Accepted: 25 October 2022

Abstract
The creation of new nanomaterials with improved characteristics, as well as the development of new approaches to obtain such materials is an urgent task in science and technology. One of the promising directions in obtaining improved nanomaterials is the use of precursors in the form of multicomponent metal nanoparticles. Thermal oxidation of bimetallic Ti/Al nanoparticles obtained by electrical explosion of wires was investigated in this work. Ti/Al nanoparticles have been found to be completely oxidized with the formation of composite TiO_2/Al_2O_3 nanoparticles after calcination at 900 °C. The formation of TiO_2 phase with a rutile structure on heating to 500 °C, and the formation of TiO_2 phases with a rutile and anatase structure, as well as α-Al_2O_3 on heating to 700 °C have been established, in addition to the residue of unoxidized metals. Complete oxidation of Ti/Al nanoparticles occurs when heated to 900 °C. The photochemical activity of TiO_2/Al_2O_3 composite nanoparticles obtained at 900 °C was studied. The degradation of methyl orange dye reached 55% under UV irradiation for 120 min.

Keywords Electrical explosion of the twisted wires · Ti/Al nanoparticles · Thermal oxidation · TiO_2/Al_2O_3 composite nanoparticles · Photochemical activity

Introduction

Nanostructured materials, nanoparticles and nanocomposites are widely used in science and technology [1–10]. In particular, metal nanoparticles are used as precursors for producing oxide nanostructures or nanocomposites [11, 12]. Titanium aluminides are often in the focus of attention when solving various problems in the field of development heat-resistant materials due to their low density, high melting point, stable physical and mechanical characteristics [13–18]. However, the behavior of titanium aluminides in the form of powders with a predominant content of the nanoscale phases has hardly been studied. Metal nanopowders can be completely oxidized in an oxygen-containing atmosphere at much lower temperatures than bulk metals and micron-sized particles, by virtue of the significant contribution of surface energy to Gibbs energy in the thermodynamic aspect [19].

As a result of the oxidation of Ti/Al nanoparticles when heating in open atmosphere, TiO_2/Al_2O_3 composite particles can be obtained, which are widely used in the processes of photodegradation of organic dyes [20–24], phenol [25], gas pollutants [26, 27], as well as polymer modifiers [28], solar cells [29], with the use being due to the high efficiency, low cost, thermal stability of such systems. As a rule, TiO_2/Al_2O_3 composite particles are obtained using sol–gel methods and subsequent heat treatment of the particles [21, 27, 30, 31]. Mesoporous Al_2O_3@TiO_2 microspheres prepared by the sol-spray pyrolysis method have showed high photocatalytic activity in the decomposition of tetracycline [32]. The introduction of amorphous γ-Al_2O_3 into the anatase TiO_2 matrix created a synergistic effect that enhanced the accumulation of tetracycline on the catalyst surface and its subsequent decomposition. Copper doped TiO_2/Al_2O_3 photocatalysts synthesized by hydrolysis of $TiCl_4$ and $AlCl_3$ have showed high catalytic activity in water splitting and in photodegradation of methylene blue dye [33]. A promising

✉ A. S. Lozhkomoev
asl@ispms.tsc.ru

[1] Institute of Strength Physics and Materials Science of Siberian Branch of Russian Academy of Sciences, 2/4, Pr. Akademicheskii, Tomsk, Russia 634055

[2] National Research Tomsk State University, 36, Lenin Ave, Tomsk, Russia 634050

Published online: 03 November 2022

method for preparing TiO_2/Al_2O_3 composite particles can be direct oxidation of Ti–Al metal nanoparticles on heating. Varying the oxidation temperature and time, it is possible to control the composition of the resulting oxidation products and evaluate the effect of the nanoparticle composition on the photochemical activity of the obtained composites.

Currently, titanium aluminide powders are produced by various methods, among which the Armstrong process [34], sodiothermic reduction process [35], mechanical milling [36], electrode induction melting gas atomization [37], and microwave sintering [38] can be distinguished. Titanium aluminides can also be obtained by the simultaneous electrical explosion of two wires (EETW) [39–41]. Changing the EETW parameters, it is possible to regulate the phase composition and particle size of the powders, while the productivity of one unit is about 200 g/h [42].

In this work the possibility of using EETW Ti/Al nanoparticles to produce composite TiO_2/Al_2O_3 nanoparticles by their oxidation in the air under heating was considered for the first time. The oxidation products obtained in the temperature range 500–1100 °C were characterized and their photochemical catalytic activity has been evaluated.

Materials and Methods

Synthesis and Oxidation of Nanoparticles

Ti/Al nanoparticles have been obtained by the electrical explosion of the twisted Ti (0.32 mm) and Al (0.25 mm) wires in an argon atmosphere (99.993%) according to the technique described previously [41]. Ti (99.7%) и Al (99.5) wires were supplied by VSMPO-AVISMA, Russia. The reactor chamber was evacuated to a residual pressure of 10^{-2} Pa, and then filled with argon to a pressure of $2•10^5$ Pa. A twist of the wires was placed in the chamber between the high-voltage and grounded electrodes. When moving twist reaches the high-voltage electrode and closes the electrical circuit, the energy stored in the capacitor bank flows through the twist resulting in heating and explosive disintegration of the wires. The nanopowder obtained was collected in a tight container, which is attached to the chamber.

Calcination was carried out in a muffle furnace SNOL 2,7/1300 (SNOL, Latvia) in air at a linear heating rate of 1 °C/min and dwelling for 4 h at temperatures of 500 °C, 700 °C, 900 °C, and 1100 °C. Nanopowder weights each 10 g were heated in corundum crucibles. The heating rate was adjusted so that no thermite reaction occurred during the heating of the weights.

Characterization of Ti/Al Nanoparticles and TiO_2/Al_2O_3 Composite Nanoparticles

The samples were characterized by transmission electron microscopy (TEM) using JEM-2100 electron microscope (JEOL, Japan) integrated with X-Max energy dispersive spectrometer (Oxford Instruments, UK). Image acquisition was performed with a 14-bit 4-megapixel side mount CCD camera Veleta G3-S04U (EMSIS GmbH, Germany). For this one drop of the sample ethanol suspension was placed on a copper grid followed by drying in air and examination at 200 kV. The phase composition and crystallographic characteristics of the samples were analyzed by X-ray diffractometry (XRD) using Shimadzu XRD-7000 with a secondary monochromator, CuKα radiation (λ = 1.542 Å) at 45 kV, 35 mA. The scans were performed in a 2θ range of 20–80 with a scan speed of $2°min^{-1}$ and scanning time of 1 s. The XRD data obtained were processed using powder diffraction file (PDF) database—PDF-2 Release 2014. The size of coherent scattering regions was determined from the Scherer equation using the XPowder 2004 software package. The broadening of the reflexeswas determined for those with the maximum intensity.The oxidation behavior of the Ti/Al nanopowder was studied using thermogravimetric analysis and differential scanning calorimetry (TG-DSC) using NETZSCH STA 449F3 (Netzsch, Waldkraiburg, Germany). The samples of 5 mg were heated in airflow from ambient temperature to 1300 °C at a heating rate of 10 °C/min.

Investigation of Photochemical Activity of TiO_2/Al_2O_3 composite

The photodegradation of methyl orange (MO) dye (MERCK, Germany) was investigated with using UV irradiation. For this, 50 mL of a dye aqueous solution with a concentration of 10 mg/L and 0.10 mg of TiO_2/Al_2O_3 composite as photocatalyst were placed in the hermetically sealed reactor. The solution was left for 30 min at room temperature until adsorption equilibrium was reached. The adsorption equilibrium reached, the suspension was irradiated under continuous agitation by UV lamp with λ = 220 nm (5.63 eV) using the BOP-01/27 (NanEMA, Russia) irradiator 10 cm away from reactor with suspension. 5 ml of the solution was taken every 10 min. The solution samples taken were centrifuged at 3500 rpm for 15 min to separate the nanoparticles from the solution. The optical density of solution at λ_{max} = 460 nm was measured using UV–Vis spectrometer SF-2000 (OKB Spectr, Russia) at ambient temperature. Each experiment was carried out in triplicate. MO photodegradation rate was determined from the decrease of the dye absorbance at λ_{max} at fixed time intervals.

Results and Discussion

Figure 1 shows images of the particles prepared by EETW of titanium and aluminum wires. As can be seen from the images, nanoparticles obtained are spherical with an average size of about 100 nm (Figs. 1a, 2a). According to the elemental analysis data the particles contain both aluminum and titanium, while the particles in which aluminum predominates (Fig. 1b, c) also are presented.

Figure 2b shows XRD pattern of the nanoparticles prepared. The peaks on this pattern belong to pure aluminum and titanium, as well as two intermetallides $AlTi_3$ and AlTi. At the same time, weak peaks of TiO are observed, which is formed when the powder is passivated with atmospheric oxygen. The phase composition of the starting particles is a consequence of particle formation mechanisms as a result of EEW. When dispersing titanium and aluminum wires, the explosion products are a homogeneous mixture of micron and submicron sized droplets of liquid metal and weakly ionized plasma. Since the specific electrical resistance of aluminum wire is significantly lower compared to titanium, more energy is injected into aluminum wire. This leads to the fact that the weakly ionized plasma includes predominantly aluminum. As a result, nano-sized particles based on the two metals (intermetallides) as well as submicron and micron sized particles mainly of titanium and aluminum are formed in the explosion products. The presence of the TiO phase is due to oxidation of micron sized titanium particles by air oxygen during passivation. The size of coherent scattering regions (D_{CSR}) for the Al phase is 67 nm, for Ti 97 nm, for TiO 29 nm, for AlTi 47 nm, for $AlTi_3$ 32 nm.

Figure 3 shows the TG-DSC curves displaying the mass gain and thermal effects that occur when Ti/Al nanoparticles are heated in an oxygen-containing atmosphere.

A monotonous growth of the sample mass and heat release is observed in the temperature range ~ 215–570 °C, which is associated with the oxidation of the nanoparticles. Further heating in the temperature range ~ 570–790 °C leads to the appearance of a set of low intensity broad peaks indicating a number of consecutive exothermic processes—oxidation of Ti and Al, the phase transformation from anatase to rutile [43], formation of Al_3Ti [44] and endothermic processes associated with the processes of sample glass transition and aluminum melting [45]. The exothermic peak at 923 °C is associated with the release of heat during oxidation of residual metal compounds in the sample, after which the mass change rate decreases and practically does not

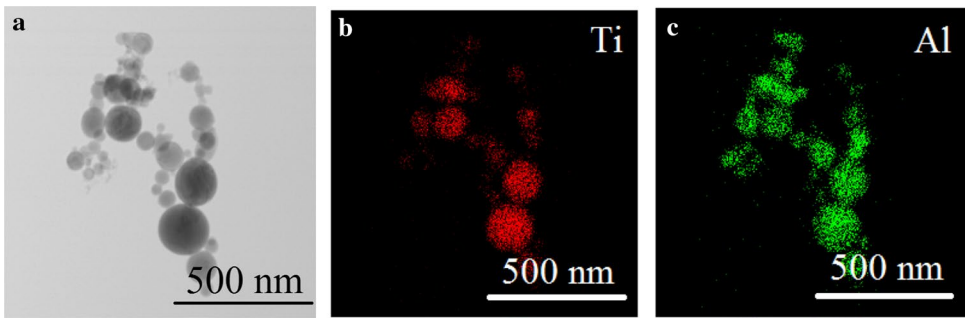

Fig. 1 TEM images (**a**) and element distribution (**b**, **c**) of Ti/Al nanoparticles: **b**—Ti; **c**—Al

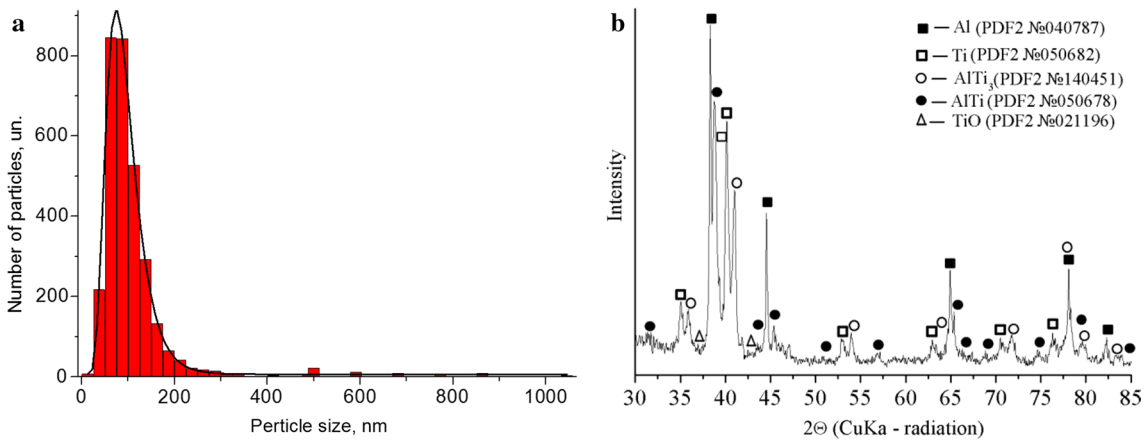

Fig. 2 Size distribution (**a**) and XRD pattern (**b**) of Ti/Al nanopowder

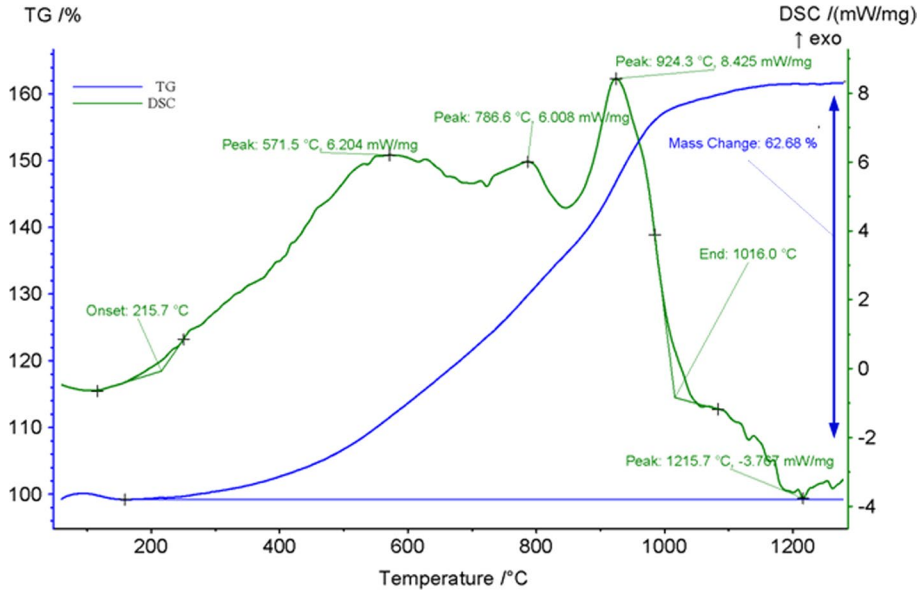

Fig. 3 TG-DSC curves of Ti/Al nanopowder

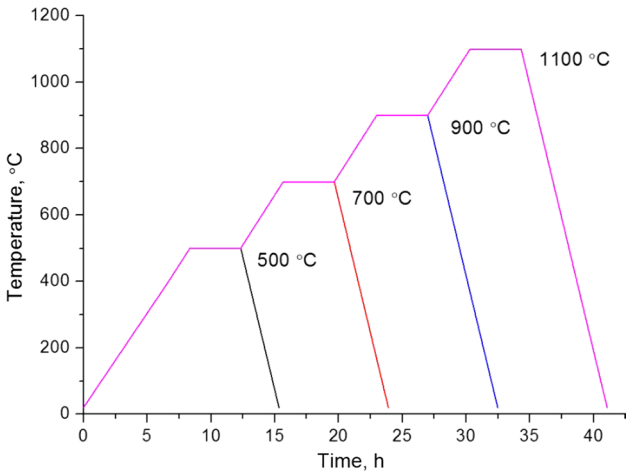

Fig. 4 Oxidation modes of Ti/Al nanopowder

change after 1100 °C, which may indicate complete oxidation of the metals.

Figure 4 shows the heating diagram of Ti-29Al nanoparticles to obtain and study the intermediate oxidation products. Nanoparticles due to their high reactivity can ignite at low temperatures, while in case of bicomponent particles the thermite reaction can be initiated [46], so the heating rate ensuring a slow uniform oxidation was selected, which was 1 °C/min. The nanoparticles were heated to temperatures in the range of 500–1100 °C at which the DSC curve (Fig. 3) showed major changes and dwelled at this temperature for 4 h.

As seen in Fig. 5a, the spherical shape of the nanoparticles after calcination at 500 °C is retained. The particles contain Ti, Al and O, as well as the particles with a predominance of Al and O are observed (Fig. 5b–d). XRD analysis shows the appearance of a polymorphic TiO_2 phase corresponding to the rutile structure. The peaks corresponding to Al_2O_3 are not observed, which may indicate low oxide content in the sample, or its X-ray amorphous state. With increasing temperature a complex character of changes in the sizes of coherent scattering regions of the corresponding phases is observed. So for Ti and Al the sizes of coherent scattering regions decrease respectively to values 83 and 59 nm, whereas for $AlTi_3$ and AlTi an increase in the sizeof coherent scattering regions to values 67 and 79 nm is observed, respectively. The described character of changes in sizes of the coherent scattering regions is most likely the result of oxidation and coalescence processes of separated individual nanoscale particles. The sizes of coherent scattering regions for Al_3Ti and TiO_2 are 21 and 18 nm, respectively.

The further oxidation of metals occurs in the temperature range of 500–700 °C, which leads to the formation of particles with a core–shell structure (Fig. 6a). This structure may be formed due to counter diffusion and interaction of oxygen and aluminum in the oxide layer of nanoparticles [47]. At the same time, according to the elemental analysis data in the mapping mode, Al, Ti and O are distributed over the entire volume of the solid phase of nanoparticles (Fig. 6b–d). Increasing the calcination temperature to 700 °C reduces the D_{CSR} of the Ti and Al phases to 73 and 52 nm, respectively. For the phases of intermetallic compounds Al_3Ti, AlTi and $AlTi_3$ the D_{CSR} decreases insignificantly relative to the previous values. For rutile and anatase phases a significant increase in D_{CSR} occurs to values of the order of 70 nm. The crystallite size of the Al_2O_3 phase does not exceed 20 nm.

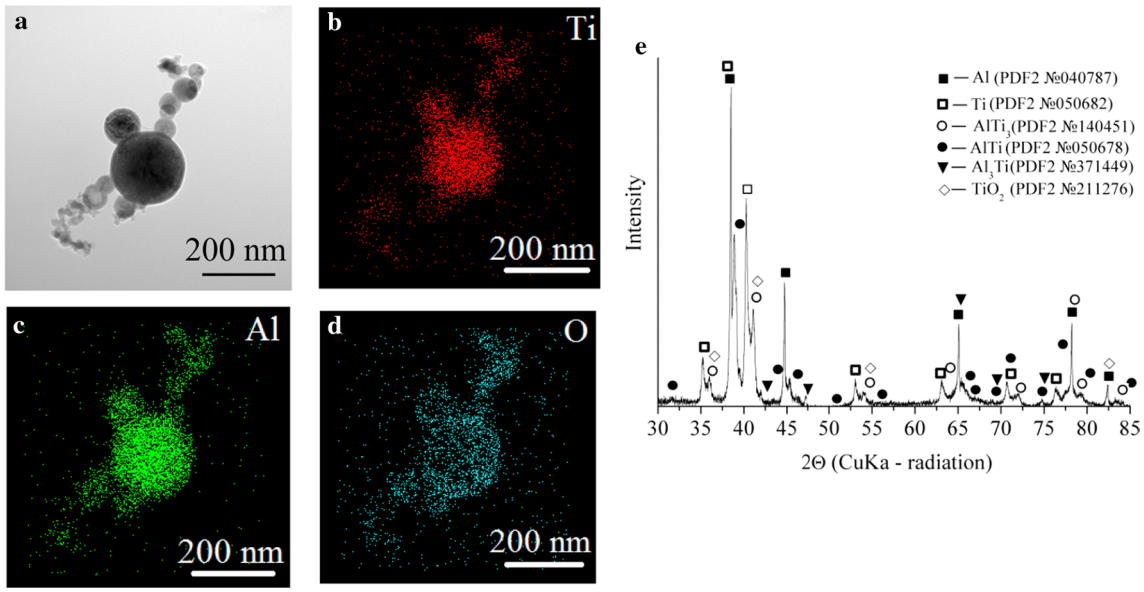

Fig. 5 TEM image (**a**), EDS mapping of Ti (**b**), Al (**c**), O (**d**) elements and XRD pattern (**e**) of the Ti/Al nanoparticles calcined at 500 °C

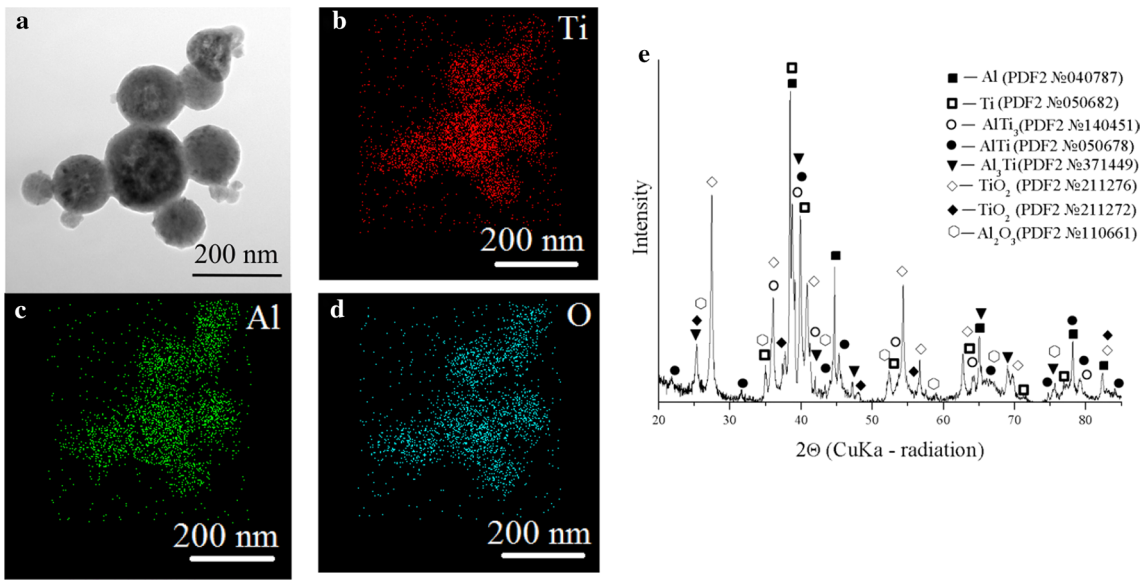

Fig. 6 TEM image (**a**), EDS mapping of Ti (**b**), Al (**c**), O (**d**) elements XRD pattern (**e**) of the nanoparticles calcined at 700 °C

The phase composition of the nanopowder after calcination at 700 °C is complemented with TiO_2 anatase structure, the intensity of rutile peaks increases, and the intensity of titanium peaks decreases (Fig. 6e). The aluminum phase is presented in the sample, which indicates a diffusion restriction in the oxide layer that prevents the interaction of aluminum with oxygen. In this case, as reported previously [47], the conversion of aluminum upon the interaction of aluminum nanoparticles with oxygen exponentially depends on the particle size.

Nevertheless, a further increase in temperature leads to complete oxidation of the nanopowder. As seen in Fig. 7, the particles acquire an irregular shape and have sharp interfaces between the phases enriched in Al or Ti (Fig. 7a–d). The XRD diffraction pattern consists of peaks corresponding to the phases TiO_2 with the rutile structure and α-Al_2O_3 (Fig. 7e).

Thus, an increase in the calcination temperature from 700 to 900 °C leads to the complete oxidation of the included metals. It has been reported that as a result of the interaction

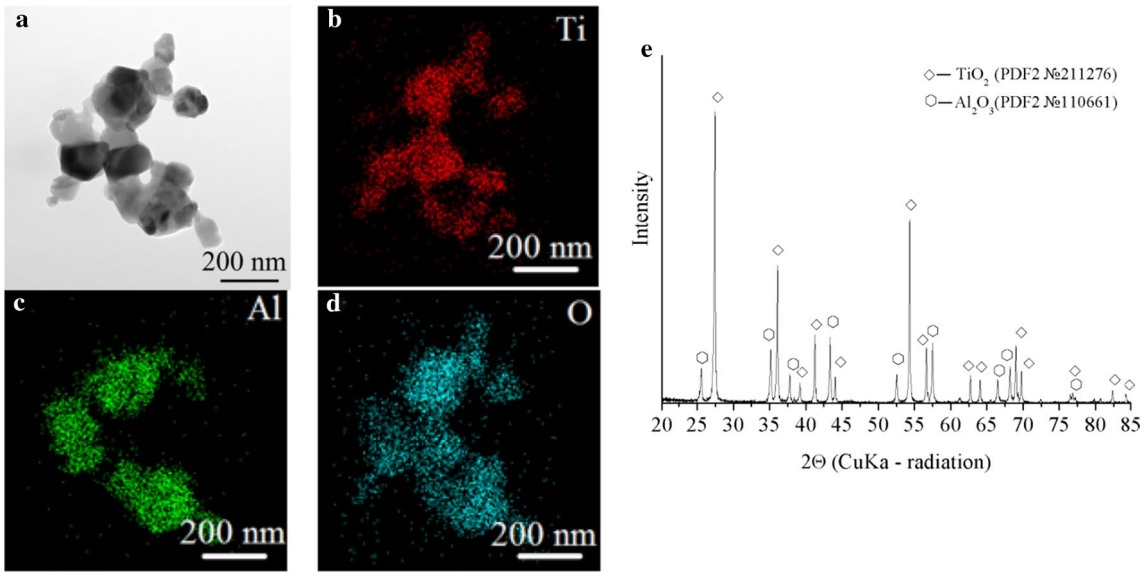

Fig. 7 TEM image (**a**), EDS mapping of Ti (**b**), Al (**c**), O (**d**) elements and XRD pattern (**e**) of the nanoparticles calcined at 900 °C

of oxygen with titanium aluminide, a simultaneous growth of titanium and aluminum oxides occurs, with TiO_2 film formed on the alloy surface, and Al_2O_3 film at the intermetallide—TiO_2 interface [48]. In this case, the diffusion of Ti cations to the particle surface is possible due to the defectiveness of alumina layer. It should also be noted that on heating the nanopowder to 800 °C, an exothermic peak is observed on the DSC curve (Fig. 3), caused by the chemical reactions of metals with oxygen with the heat release, which contributes to the intensification of the oxidation process of metal phases.

A further increase in temperature to 1100 °C does not lead to significant changes in the morphology and composition of nanoparticles resulted (Fig. 8), while the size of coherent scattering regions D_{CSR} increases for TiO_2 from 75 to 88 nm, for α-Al_2O_3 from 67 to 122 nm.

Increase in the D_{CSR} for α-Al_2O_3 and TiO_2 causes a decrease in such defects as grain boundaries, which affect the photochemical activity of the materials [49].

The results obtained indicate that, in contrast to bulk alloys, the EETW Ti/Al nanoparticles can be completely oxidized with the formation of TiO_2-Al_2O_3 composite at a

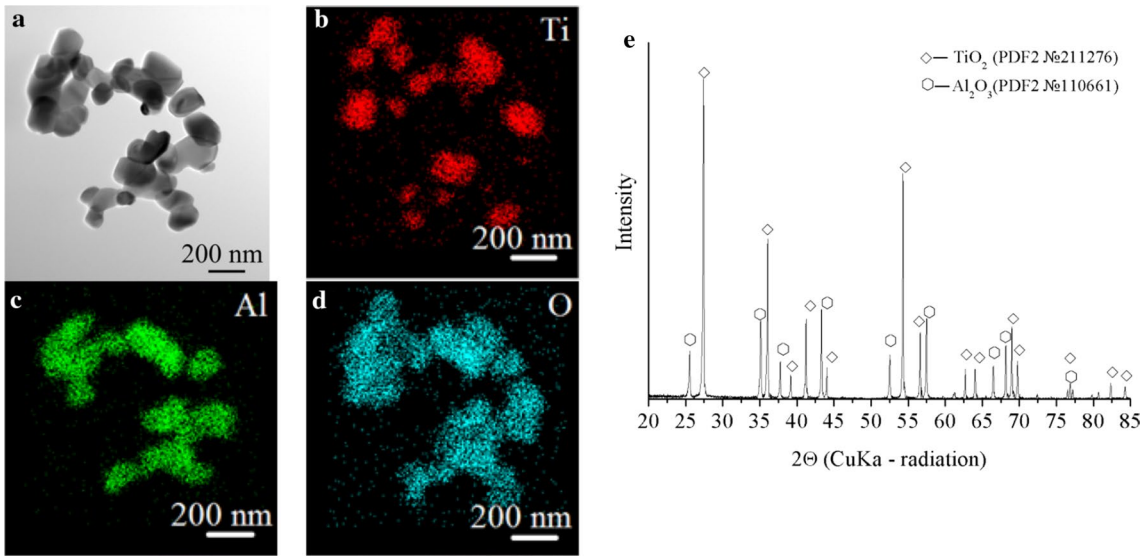

Fig. 8 TEM image (**a**), EDS mapping of Ti (**b**), Al (**c**), O (**d**) elements and XRD pattern (**e**) of the nanoparticles calcined at 1100 °C

temperature of 900 °C. Moreover, such particles have multiple phase boundaries, which can contribute to an increase in their photochemical activity.

Using FT-IR spectroscopy, the surface of the samples obtained was studied (Fig. 9a). All samples are characterized by bands at 3450 cm^{-1} and at 1640 cm^{-1}, which can be assigned to the stretching modes and bending vibration of the adsorbed water [50, 51]. The broad band in the region of 500–750 cm^{-1} for Ti/Al and samples calcined at 500 and 700 °C (Fig. 9, curves 1, 2, 5) is assigned to Ti–O–Ti bond of a titanium oxide and AlO_6 octahedra, whereas the shoulder at 890 cm^{-1} is assigned to AlO_4 tetrahedra [52, 53]. Increasing the calcination temperature to 900–1100 °C leads to the appearance of pronounced band at 660 cm^{-1} corresponding to the Ti–O–Ti stretching vibration mode. In addition, strong peaks at 583 cm^{-1} and 439 cm^{-1} are observed, which refer to the vibration of Ti–O–Al linkage which formed by the interaction between Ti group and Al group [50].

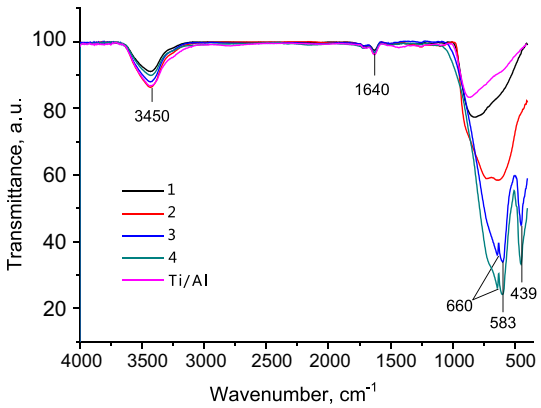

Fig. 9 FT-IR spectra of Ti/Al nanoparticles (curve Ti/Al) and composit nanoparticles after calcinations of Ti/Al at 500 °C (curve 1), 700 °C (curve 2), 900 °C (curve 3) and 1100 °C (curve 4)

Photoinduced photodegradation of MO dye was used to evaluate the photocatalytic activity of TiO_2/Al_2O_3 composite nanoparticles. The concentration of MO dye in the absence of nanoparticles practically did not change during the experiment; therefore, the photoinduced self-decomposition of the dye was neglected. Degradation of MO dye in the presence of TiO_2/Al_2O_3 composite nanoparticles was considered as a result of photocatalytic reaction.

The kinetic curves of MO degradation catalyzed by TiO_2/Al_2O_3 nanoparticles are shown in Fig. 10. All TiO_2/Al_2O_3 composite nanoparticles showed obvious photocatalytic activity. The highest photocatalytic activity was demonstrated by the sample obtained after oxidation of Ti/Al nanoparticles at 900 °C. In this case, the efficiency of MO degradation reached 55% after 120 min of UV irradiation.

Figure 9 shows linearized plots of the MO concentration versus time. All plots show good linear correlation (Fig. 10b), and the values of the determination coefficients R^2 for all cases are close to 1, which may indicate that the MO degradation reaction can be described by pseudo first order kinetics (1):

$$-\ln\left(C_t/C_0\right) = kt \tag{1}$$

where C_0—initial concentration, C_t—concentration at time t; k—degradation rate constant.

The results obtained (Fig. 7e) show that the sample calcined at 900 °C does not contain intermetallide phases that do not participate in the charge carrier transfer processes, TiO_2 is more active in the photocatalytic reaction. A further increase in the calcination temperature led to an increase in particle size and a decrease in the number of the surface

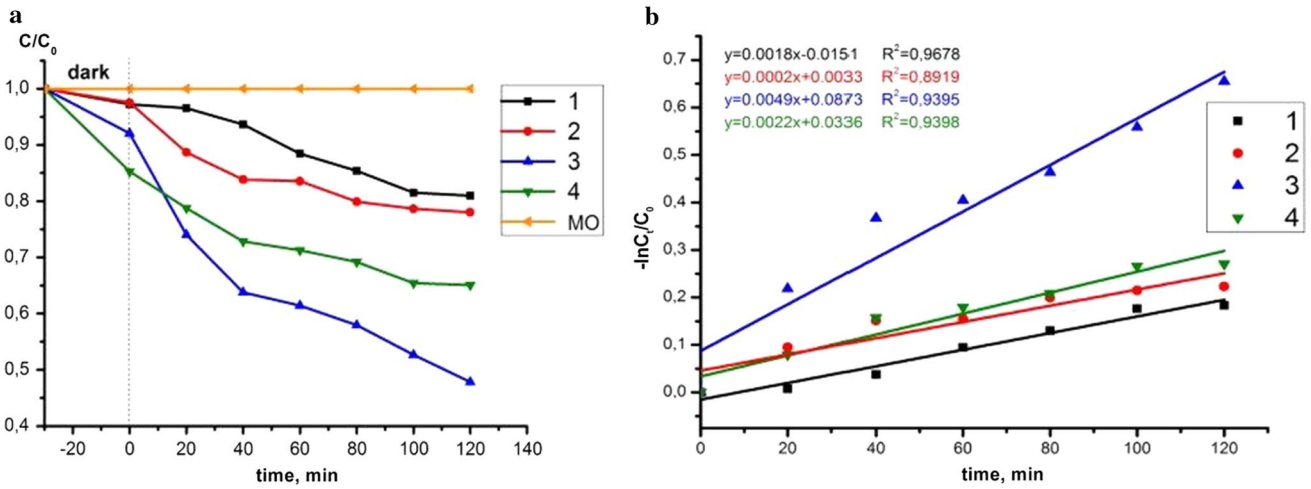

Fig. 10 Kinetic plots of MO degradation (**a**) and linearized plots of the pseudo-first order reaction model (**b**) for TiO_2/Al_2O_3 composite nanoparticles after oxidation at 500 °C (curve 1), 700 °C (curve 2), 900 °C (curve 3) and 1100 °C (curve 4)

defects. Based on [54], co-presence of Al_2O_3 and TiO_2 in the particles leads to a synergistic effect. TiO_2, when interacting with water under UV irradiation, generates electrons that can be transferred to the defective levels of Al_2O_3. In turn, the holes on the TiO_2 surface react with OH^- ions or H_2O molecules to form ·OH hydroxyl radicals oxidizing MO. As the calcination temperature increases from 500 to 900 °C the MO degradation reaction rate increases significantly from 0.0151 to 0.0873 s^{-1}.

The mechanism of MO photodegradation in the presence of TiO_2/Al_2O_3 composite nanoparticles can be described as follows. During UV irradiation, photoinduced electrons move from the valence band of TiO_2 to its conduction band. After that they can either recombine with holes, or react with oxygen to form O_2^- or as shown by the authors [55] to move to defective levels of Al_2O_3, despite the fact that the conduction band potential (CB potential) of Al_2O_3 is higher than that of TiO_2. The transfer of photoinduced electrons to defective levels promotes the spatial separation of electrons and holes and increases the photocatalytic activity of the nanoparticles. Schematically the mechanism of MO photodegradation is shown in Fig. 11.

The results obtained demonstrate the possibility to synthetize TiO_2/Al_2O_3 composite nanoparticles by oxidation of electroexplosive bimetallic Ti/Al nanoparticles. Depending on the oxidation mode, nanoparticles of various compositions can be obtained. It should be noted that the TiO_2 moieties included in the sample with the highest photocatalytic activity have a rutile structure, which is less catalytically active than anatase structure [56]. The synthesized nanoparticles can also be used as catalyst carriers, functional additives in polymeric materials, in purification systems, medicine, etc.

Conclusion

Ti/Al nanoparticles obtained by simultaneous electrical explosion of Ti and Al wires in an inert atmosphere can be used to obtain TiO_2/Al_2O_3 composites by slow heating of the Ti/Al nanoparticles in open atmosphere.

The main changes in the morphology and composition of nanoparticles occur in the temperature range of 500–900 °C, accompanied by the formation of intermetallic Al_3Ti, Al_2O_3 and TiO_2 both anatase and rutil structures. Increasing the calcination temperature up to 900 °C the complete oxidation of metals occurs with the formation of composite nanoparticles, which include rutile TiO_2 and α-Al_2O_3. Upon further heating up to 1100 °C the phase composition does not change, while the degree of crystallinity (D_{scr}) of the oxides increases. The formation of thermodynamically stable oxides already at 900 °C is caused, in our opinion, by the release of additional heat due to the exothermic reaction of metals with oxygen, which, according to DSC data, begins from ~ 850 °C.

The photochemical activity of the synthesized composite particles was evaluated. The greatest photocatalytic activity in UV-induced MO dye degradation was exhibited by TiO_2/Al_2O_3 composite nanoparticles obtained at 900 °C, which include TiO_2 with a rutile structure and α-Al_2O_3. After

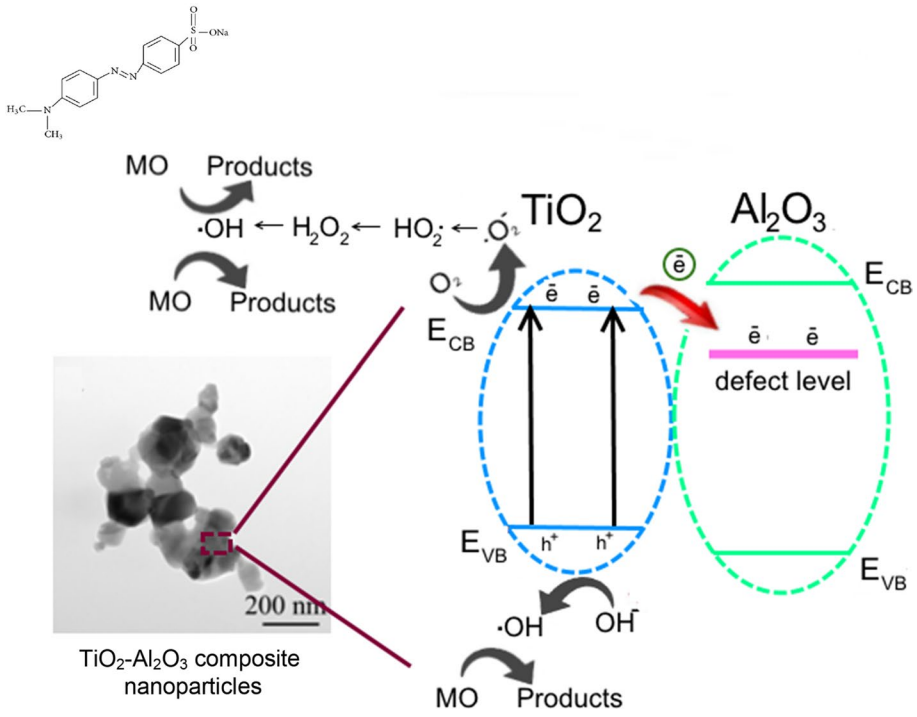

Fig. 11 Schematic diagram of mechanism for the photocatalytic MO degradation over TiO_2/Al_2O_3 composite nanoparticles

60 min of UV irradiation, the degradation efficiency of MO dye was 55%. The sample obtained at 900 °C is the most active in MO degradation due to the absence of metals not involved in the charge carrier transfer, as well as due to a greater number of defects in the Al_2O_3 structure, compared to the sample obtained at 1100 °C.

Acknowledgements Ti–Al nanoparticles were obtained and studied within the framework of a project of the Russian Science Foundation (Grant No. 21-79-30006). The study of the photochemical activity of Ti-Al nanoparticle oxidation products was performed according to the Government research assignment for ISPMS SB RAS, project FWRW-2022-0002.

Declarations

Conflict of interest On behalf of all authors, the corresponding author states that there are no conflicts of interest.

References

1. R. Monsef, M. Ghiyasiyan-Arani, and M. Salavati-Niasari (2021). Design of magnetically recyclable ternary Fe_2O_3/$EuVO_4$/g-C_3N_4 nanocomposites for photocatalytic and electrochemical hydrogen storage. *ACS Appl. Energy Mater.* **4** (1), 680–695.
2. M. Salavati-Niasari and F. Davar (2006). In situ one-pot template synthesis (IOPTS) and characterization of copper (II) complexes of 14-membered hexaaza macrocyclic ligand "3, 10-dialkyldibenzo-1, 3, 5, 8, 10, 12-hexaazacyclotetradecane." *Inorg. Chem. Commun.* **9** (2), 175–179.
3. S. Ahmadian-Fard-Fini, D. Ghanbari, O. Amiri, and M. Salavati-Niasari (2020). Electro-spinning of cellulose acetate nanofibers/Fe/carbon dot as photoluminescence sensor for mercury (II) and lead (II) ions. *Carbohydrate Polymers* **229**, 115428.
4. M. Amiri, M. Salavati-Niasari, A. Pardakhty, M. Ahmadi, and A. Akbari (2017). Caffeine: A novel green precursor for synthesis of magnetic $CoFe_2O_4$ nanoparticles and pH-sensitive magnetic alginate beads for drug delivery. *Mater. Sci. Eng: C* **76**, 1085–1093.
5. S. Zinatloo-Ajabshir, M. S. Morassaei, O. Amiri, M. Salavati-Niasari, and L. K. Foong (2020). $Nd_2Sn_2O_7$ nanostructures: green synthesis and characterization using date palm extract, a potential electrochemical hydrogen storage material. *Ceram. Int.* **46** (11), 17186–17196.
6. F. Motahari, M. R. Mozdianfard, and M. Salavati-Niasari (2015). Synthesis and adsorption studies of NiO nanoparticles in the presence of H2acacen ligand, for removing Rhodamine B in wastewater treatment. *Process Saf. Environ. Prot.* **93**, 282–292.
7. S. Zinatloo-Ajabshir and M. Salavati-Niasari (2019). Preparation of magnetically retrievable $CoFe_2O_4$@ SiO_2@ $Dy2Ce_2O_7$ nanocomposites as novel photocatalyst for highly efficient degradation of organic contaminants. *Compos. Part B Eng.* **174**, 106930.
8. S. Zinatloo-Ajabshir, S. Mortazavi-Derazkola, and M. Salavati-Niasari (2018). Nd_2O_3-SiO_2 nanocomposites: a simple sonochemical preparation, characterization and photocatalytic activity. *Ultrason. Sonochem.* **42**, 171–182.
9. F. Davar, M. Salavati-Niasari, and Z. Fereshteh (2010). Synthesis and characterization of SnO_2 nanoparticles by thermal decomposition of new inorganic precursor. *J. Alloys Compd.* **496** (1–2), 638–643.
10. M. Hassanpour, H. Safardoust-Hojaghan, and M. Salavati-Niasari (2017). Degradation of methylene blue and Rhodamine B as water pollutants via green synthesized Co_3O_4/ZnO nanocomposite. *J. Mol. Liq.* **229**, 293–299.
11. A. S. Lozhkomoev, E. A. Glazkova, O. V. Bakina, M. I. Lerner, I. Gotman, E. Y. Gutmanas, et al. (2016). Synthesis of core–shell AlOOH hollow nanospheres by reacting Al nanoparticles with water. *Nanotechnology* **27** (20), 205603.
12. A. S. Lozhkomoev, N. G. Rodkevich, A. B. Vorozhtsov, and M. I. Lerner (2020). Oxidation and oxidation products of encapsulated aluminum nanopowders. *J. Nanopart. Res.* **22** (1), 1–13.
13. S. Lyu, Y. Sun, L. Ren, W. Xiao, and C. Ma (2017). Simultaneously achieving high tensile strength and fracture toughness of Ti/Ti–Al multilayered composites. *Intermetallics* **90**, 16–22.
14. S. Djanarthany, J. C. Viala, and J. Bouix (2001). An overview of monolithic titanium aluminides based on Ti_3Al and TiAl. *Mater. Chem. Phys.* **72** (3), 301–319.
15. M. Peters, J. Kumpfert, C. H. Ward, and C. Leyens (2003). Titanium alloys for aerospace applications. *Adv. Eng. Mater.* **5** (6), 419–427.
16. W. Zhang, W. Li, H. Zhai, Y. Wu, S. Wang, G. Liang, and R. J. Wood (2020). Microstructure and tribological properties of laser in-situ synthesized Ti_3Al composite coating on Ti-6Al-4V. *Surf. Coatings Technol.* **395**, 125944.
17. T. Zhang, G. Fan, K. Miao, K. Chen, Z. Pan, S. Chen, et al. (2017). Bimodal laminated Ti_3Al matrix composite achieved by in situ formed Ti_5Si_3 reinforcements. *Mater. Sci. Eng. A* **707**, 419–425.
18. A. V. Bakulin, S. S. Kulkov, and S. E. Kulkova (2021). Adhesion properties of clean and doped Ti_3Al/Al_2O_3 interface. *Appl. Surf. Sci.* **536**, 147639.
19. P. A. Chernavskii, N. V. Peskov, A. V. Mugtasimov, and V. V. Lunin (2007). Oxidation of metal nanoparticles: Experiment and model. *Russ. J. Phys. Chem. B* **1** (4), 394–411.
20. W. Zhang, C. Li, and R. Li (2015). Sol–gel preparation of TiO_2–Al_2O_3 composite materials to promote photocatalytic activity. *Nanosci. Nanotechnol. Asia* **5** (1), 8–14.
21. W. J. Zhang and H. L. Xin (2012). Porous TiO_2-Al_2O_3 photocatalyst: The effects of calcination time. *Adv. Mater. Res.* **496**, 165–168.
22. R. Ahmad, J. K. Kim, J. H. Kim, and J. Kim (2018). Effect of polymer template on structure and membrane fouling of TiO_2/Al_2O_3 composite membranes for wastewater treatment. *J. Ind. Eng. Chem.* **57**, 55–63.
23. J. L. Luo, S. F. Wang, W. Liu, C. X. Tian, J. W. Wu, X. T. Zu, et al. (2017). Influence of different aluminum salts on the photocatalytic properties of Al doped TiO_2 nanoparticles towards the degradation of AO_7 dye. *Sci. Rep.* **7** (1), 1–16.
24. D. Zhao, C. Chen, Y. Wang, W. Ma, J. Zhao, T. Rajh, and L. Zang (2008). Enhanced photocatalytic degradation of dye pollutants under visible irradiation on Al (III)-modified TiO_2: Structure, interaction, and interfacial electron transfer. *Environ. Sci. Technol.* **42** (1), 308–314.
25. C. Anderson and A. J. Bard (1997). Improved photocatalytic activity and characterization of mixed TiO_2/SiO_2 and TiO_2/Al_2O_3 materials. *J. Phys. Chem. B* **101** (14), 2611–2616.
26. J. Pei, W. Ma, R. Li, Y. Li, and H. Du (2015). Preparation and photocatalytic properties of TiO_2–Al_2O_3 composite loaded catalysts. *J Chem*. https://doi.org/10.1155/2015/806568.
27. M. Polat, A. M. Soylu, D. A. Erdogan, H. Erguven, E. I. Vovk, and E. Ozensoy (2015). Influence of the sol–gel preparation method on the photocatalytic NO oxidation performance of TiO_2/Al_2O_3 binary oxides. *Catal. Today* **241**, 25–32.
28. F. Z. Yakdoumi and A. S. Hadj-Hamou (2020). Effectiveness assessment of TiO2-Al_2O_3 nano-mixture as a filler material for improvement of packaging performance of PLA nanocomposite films. *J. Polym. Eng.* **40** (10), 848–858.
29. S. Wu, H. Han, Q. Tai, J. Zhang, S. Xu, C. Zhou, et al. (2008). Improvement in dye-sensitized solar cells employing TiO_2

electrodes coated with Al_2O_3 by reactive direct current magnetron sputtering. *J. Power Sour.* **182** (1), 119–123.
30. M. Andrianainarivelo, R. J. Corriu, D. Leclercq, P. H. Mutin, and A. Vioux (1997). Nonhydrolytic sol−gel process: Aluminum titanate gels. *Chem. Mater.* **9** (5), 1098–1102.
31. E. Celik, I. Keskin, I. Kayatekin, F. A. Azem, and E. Özkan (2007). Al2O3–TiO2 thin films on glass substrate by sol–gel technique. *Mater. Characteriz.* **58** (4), 349–357.
32 T. K. Vo (2022). Spray pyrolysis synthesis and UV-driven photocatalytic activity of mesoporous Al_2O_3@ TiO_2 microspheres. *Environ Sci Pollut Res*. https://doi.org/10.1007/s11356-022-18865-0.
33. Y. F. Jatoi, M. Fiaz, and M. Athar (2021). Synthesis of efficient TiO_2/Al_2O_3@ Cu (BDC) composite for water splitting and photodegradation of methylene blue. *J. Aust. Ceram. Soc.* **57** (2), 489–496.
34. W. Chen, Y. Yamamoto, W. H. Peter, S. B. Gorti, A. S. Sabau, M. B. Clark, et al. (2011). Cold compaction study of Armstrong process® Ti–6Al–4V powders. *Powder Technol.* **214** (2), 194–199.
35. C. Du, J. Xiao, B. Zhang, and H. Zhu (2021). Facile synthesis of fine Ti–Al intermetallic compound powders via sodiothermic reduction in molten CaCl2. *Intermetallics* **129**, 107038.
36. K. A. Annan, P. Daswa, K. Motumbo, and C. W. Siyasiya (2021). Influence of milling parameters on the structural and phase formation in Ti-20% Al alloy through mechanical milling. *Mater. Today Proc.* **38**, 779–783.
37. B. Liu, M. Wang, Y. Du, and J. Li (2020). Size-dependent structural properties of a high-Nb TiAl alloy powder. *Materials* **13** (1), 161.
38. W. Chen, J. Tang, X. Shi, N. Ye, Z. Yue, and X. Lin (2020). Synthesis and formation mechanism of high purity Ti_3AlC_2 powders by microwave sintering. *Int. J. Appl. Ceram. Technol.* **17** (2), 778–789.
39. A. V. Pervikov, S. O. Kazantsev, A. S. Lozhkomoev, and M. I. Lerner (2020). Bimetallic Al/Ag, Al/Cu and Al/Zn nanoparticles with controllable phase compositions prepared by the electrical explosion of two wires. *Powder Technol.* **372**, 136–147.
40. A. V. Pervikov, K. V. Suliz, and M. I. Lerner (2020). Nanoalloying of clusters of immiscible metals and the formation of bimetallic nanoparticles in the conditions of non-synchronous explosion of two wires. *Powder Technol.* **360**, 855–862.
41. M. Lerner, A. Pervikov, E. Glazkova, N. Rodkevich, and N. Toropkov (2021). Electrical explosion synthesis, oxidation and sintering behavior of Ti–Al intermetallide powders. *Metals* **11** (5), 760.
42. A. S. Lozhkomoev, A. V. Pervikov, S. O. Kazantsev, A. F. Sharipova, N. G. Rodkevich, N. E. Toropkov, et al. (2021). Synthesis of Fe/Fe_3O_4 core-shell nanoparticles by electrical explosion of the iron wire in an oxygen-containing atmosphere. *J. Nanopart. Res.* **23** (3), 1–12.
43. S. Qiu and S. J. Kalita (2006). Synthesis, processing and characterization of nanocrystalline titanium dioxide. *Mater. Sci. Eng. A* **435**, 327–332.
44 Z. R. Yang, S. Q. Wang, X. H. Cui, Y. T. Zhao, M. J. Gao, and M. X. Wei (2008). Formation of Al3Ti/Mg composite by powder metallurgy of Mg–Al–Ti system. *Sci Technol Adv Mater*. https://doi.org/10.1088/1468-6996/9/3/035005.
45. P. Urban, F. Ternero, E. S. Caballero, S. Nandyala, J. M. Montes, and F. G. Cuevas (2019). Amorphous Al–Ti powders prepared by mechanical alloying and consolidated by electrical resistance sintering. *Metals* **9** (11), 1140.
46. V. P. Kobyakov and T. V. Barinova (2011). Combustion of TiO_2-Al thermit mixtures containing C and Cs in air: Phase composition of products. *Int. J. Self-Propag. High-Temp. Synth.* **20** (3), 161–165.
47. O. Rai, K. Park, L. Zhou, and M. R. Zachariah (2006). Understanding the mechanism of aluminium nanoparticle oxidation. *Combust. Theory Modelling* **10** (5), 843–859.
48. V. Maurice, G. Despert, S. Zanna, P. Josso, M. P. Bacos, and P. Marcus (2007). XPS study of the initial stages of oxidation of α2-Ti_3Al and γ-TiAl intermetallic alloys. *Acta Mater.* **55** (10), 3315–3325.
49. M. Kamei (2008). Localization of the photocatalytic reaction on the grain boundary of bicrystalline TiO_2. *Appl. Phys. Express* **1** (10), 101201.
50. M. A. Ahmed and M. F. Abdel-Messih (2011). Structural and nano-composite features of TiO_2–Al_2O_3 powders prepared by sol–gel method. *J. Alloys Compd.* **509** (5), 2154–2159.
51. Q. Zhu, H. Duan, B. Lin, Y. Zhu, Y. Hu, and Y. Zhou (2019). Higher acetone conversion obtained over a TiO_2–Pd bifunctional catalyst for liquid-phase synthesis of methyl isobutyl ketone: The role of Al_2O_3 support. *Catal. Lett.* **149** (9), 2636–2644.
52. G. Urretavizcaya, A. L. Cavalieri, J. M. Lopez, I. Sobrados, and J. Sanz (1998). Thermal evolution of alumina prepared by the sol-gel technique. *J. Mater. Synth. Process.* **6** (1), 1–7.
53. M. J. Velasco, F. Rubio, J. Rubio, and J. L. Oteo (1999). DSC and FT-IR analysis of the drying process of titanium alkoxide derived precipitates. *Thermochimica Acta* **326** (1–2), 91–97.
54. A. A. Ismail, I. Abdelfattah, M. F. Atitar, L. Robben, H. Bouzid, S. A. Al-Sayari, and D. W. Bahnemann (2015). Photocatalytic degradation of imazapyr using mesoporous Al_2O_3–TiO_2 nanocomposites. *Sep. Purif. Technol.* **145**, 147–153.
55. F. Li, et al. (2012). N-doped P25 TiO2–amorphous Al2O3 composites: One-step solution combustion preparation and enhanced visible-light photocatalytic activity. *J. Hazard. Mater.* **239**, 118–127.
56. T. Luttrell, S. Halpegamage, J. Tao, A. Kramer, E. Sutter, and M. Batzill (2014). Why is anatase a better photocatalyst than rutile?-Model studies on epitaxial TiO2 films. *Sci. Rep.* **4** (1), 1–8.